Completing Dental Models While Preserving Crown Geometry and Meshing Topology

Hao Yu
Shandong University
No.72 Binhai Rd, Qingdao, Shandong, China
yuh@mail.sdu.edu.cn

Ruian Wang
Shandong University
No.72 Binhai Rd, Qingdao, Shandong, China
wra.time@gmail.com

Longdu Liu
Shandong University
No.72 Binhai Rd, Qingdao, Shandong, China
tanakaazkatana@gmail.com

Shuangmin Chen
Qingdao University of Science and Technology
No.99 Songling Rd, Qingdao, Shandong, China
csmqq@163.com

Shiqing Xin
Shandong University
No.72 Binhai Rd, Qingdao, Shandong, China
xinshiqing@sdu.edu.cn

Zhenyu Shu
NingboTech University
No.1 Qianhu South Rd, Ningbo, Zhejiang, China
shuzhenyu@nit.zju.edu.cn

Changhe Tu
Shandong Uzniversity
No.72 Binhai Rd, Qingdao, Shandong, China
chtu@sdu.edu.cn

Abstract

In the field of digital orthodontics, dental models with complete roots are essential digital assets, particularly for visualization and treatment path planning. However, oral scans can only capture dental crowns, leaving the roots missing. In this paper, we introduce a meticulously designed algorithm pipeline to complete dental models while preserving the crown geometry and mesh topology. Our pipeline begins with a learning-based point cloud completion for the existing dental crowns. We then reconstruct a complete tooth, including both the crown and root, to guide subsequent operations. Following this, we restore the crown's geometry and mesh topology based on a kind of strong-Delaunay meshing structure. Finally, we optimize the transition zone between the crown and root by biharmonic smoothing. A key advantage of our algorithm is that the completed tooth model accurately preserves the geometry and mesh topology of the original crown while ensuring high-quality triangulation in the dental roots. Extensive experiments have shown that our algorithm can generate the corresponding root based on the given crown and integrate them, while preserving the integrity of the crown area.

Keywords: Digital Orthodontics, Point Cloud Completion, Implicit Reconstruction, Mesh Integration, Restricted Voronoi Diagram

1. Introduction

Digital orthodontics [31] refers to the integration of digital technology into the diagnosis, treatment planning, and management of orthodontic problems. Generally speaking, the process includes several steps, starting with an oral scan and culminating in the generation of a detailed treatment planning solution [30]. Digital orthodontics enhances the patient experience by making treatments quicker, less invasive, and more precise. It also provides orthodontists with the tools to deliver high-quality care with better outcomes.

Among the many processes involved in digital orthodontics, tooth segmentation is a critical step that primarily involves separating the dental crown from the gingiva and identifying each dental crown. Traditional tooth segmentation techniques [43] begin with shape analysis (e.g., curvature) to identify the boundaries where one tooth meets another or meets the gum line. Following this, individual teeth are segmented using clustering techniques, graph-based methods, or other classification approaches. The advent of deep learning has significantly enhanced tooth segmentation, with Convolutional Neural Networks leading the advancements [7, 37]. Regardless of whether traditional or deep learning-based methods are used, the outputs generally consist of dental crowns depicted as open mesh surfaces, lacking dental roots. This limitation poses challenges in subsequent steps. For instance, when planning how one tooth moves from its initial position to the target posture, it is necessary to avoid collisions between successive dental roots. Additionally, the completion of teeth can provide a better visualization of the occlusion status. Therefore, tooth completion is a crucial task in digital orthodontics.

Several studies have concentrated on the completion of dental models. Martorelli and Ausiello [24] utilized five human posterior molars from micro-computed tomography (CT) scans as reference models and developed specific computer-aided design procedures for completing dental models. However, the resulting dental roots are still absent, differing significantly from actual conditions. The advancement of deep learning technology [45, 21] now allows for the generation of complete tooth models with simulated roots that do not depend on cone beam computed tomography(CBCT) data, resulting in accurate and natural tooth shapes. Despite these advancements, the critical challenge of accurately preserving dental crowns remains unaddressed.

To this end, we establish the goals of this paper. Given a polygonal crown model without root, our task is to recover the complete tooth model with high-fidelity dental roots. Additionally, we set three specific requirements: First, the geometry and topology of the digital crown must be preserved. Second, there should be a visually natural transition between the crown and the roots. Finally, the completed model must feature high-quality triangulation.

To meet the aforementioned requirements, we have developed a set of novel techniques to tackle these challenges. Our algorithm initiates with a point cloud completion stage, following the dental crown prior, where a set of points believed to be on the dental root is generated. Subsequently, we quickly reconstruct a surface to obtain a guiding surface that roughly represents the completed shape. However, this process does not fully respect the given crown shape. Specifically, the geometry and mesh topology of the dental crown are altered. To address this issue, we introduce a strong-Delaunay meshing structure, whose meshing topology remains unchanged in terms of restricted surface Voronoi decomposition. This observation helps us restore the crown geometry and mesh topology. Finally, our algorithm ends with optimizing the transition zone between the crown and root by biharmonic smoothing.

To summarize, our contributions are threefold:

1. We introduce an algorithmic framework to complete a tooth model from a dental crown. Experimental results demonstrate that our completion algorithm can accurately recover high-fidelity dental roots.

2. We propose a new kind of meshing structure, named *strong-Delaunay* mesh in this paper, which helps maintain the geometry and mesh topology of the given dental crown, a method not previously reported in the existing literature.

3. We employ a set of strategies to enhance the shape appearance of the completed teeth, including identifying the skirt of a crown and applying biharmonic smoothing to the transition area. Specifically, by combining Poisson reconstruction with tetrahedral tiling, we achieve both high triangulation quality and a faithful reconstruction outcome.

2. Related Works

In this section, we primarily review two types of research work: shape completion and remeshing.

2.1. Shape Completion

The completion of incomplete shapes is an important process in the field of geometric processing. The goal of completing shapes is to derive or restore missing or incomplete parts based on available information or prior knowledge. If the missing regions are tiny compared to the known parts, hole-filling algorithms can solve this problem. Conventional shape completion algorithms can be divided into two main methods: volumetric and surface-based.

Volumetric-based methods [2, 20, 3] rely on volumetric structures such as regular 3D grids, octrees, tetrahedral subdivisions, or sparser volume samplings. These structures provide information about the interior and exterior of the object, which is essential for completing the shape. Techniques commonly used in volumetric-based methods include voxel-based interpolation, implicit surface reconstruction, and volumetric shape synthesis. Surface-based methods [34, 35, 13, 42], on the other hand, focus on the properties of the surface, such as boundary topology or curvature. These methods use known surface information to infer or generate the missing parts and typically involve surface reconstruction algorithms, mesh generation, or surface interpolation techniques.

Shape completion also plays a vital role in orthodontics. Due to the limited availability of CBCT devices, many cases in digital dental treatment lack authentic patient root data from CT images. Nonetheless, accurately predicted root models are crucial for assisting dentists and technicians in treatment planning. They help avoid excessive translation or rotation of tooth designs, reducing the risk of bone fenestration or cracking during treatment. Consequently, generating reasonable and aesthetically pleasing root data is

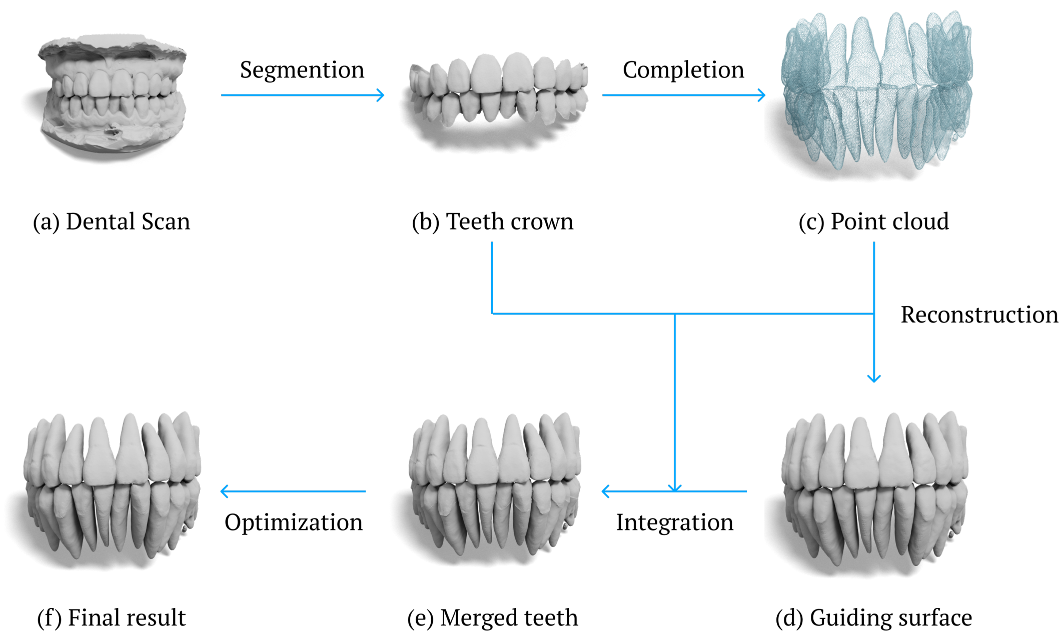

Figure 1. The pipeline of our method.

essential during tooth completion process, which supports subsequent digital diagnosis and treatment procedures. For example, Qian et al. [27] leveraged prior knowledge of tooth models for their completion. Initially, they conducted layer-wise slicing to obtain boundary points for each layer. They then used C2 continuous B-spline interpolation to connect two adjacent boundary points. Despite advancements in deep learning technology [45, 21], a significant challenge remains: the scarcity of comprehensive 3D dental datasets. In our implementation, we employ AdaPoinTr [40], a state-of-the-art point cloud completion model, and generate a dataset using data augmentation techniques.

2.2. Mesh Extraction and Remeshing

Mesh extraction often serves as the subsequent step in the task of implicit reconstruction. The most common technique for mesh extraction is marching cubes. Most implicit reconstruction approaches, such as Poisson reconstruction [16] and its variants [15, 17, 44], Moving Least Squares [19], and Ball Pivoting [1], require a mesh extraction step.

On the other hand, remeshing assumes that the input is a polygonal mesh surface and involves altering the mesh topology. Remeshing can be performed using various methods, including local modification [10, 18, 6, 8], Delaunay triangulation [4, 23, 12], optimization [36, 5, 28], and Centroidal Voronoi Tessellation [9, 39, 25, 38].

Generally speaking, mesh extraction and remeshing are distinct tasks, each useful in different scenarios. However, both stages are typically necessary when the output mesh requires high-quality triangulations. This process can lead to the accumulation of errors. A growing research trend focuses on directly extracting high-quality mesh surfaces from an implicit field. Hass et al. [14] present a method for approximating an implicit surface with a piecewise-flat triangulated surface, where the triangles are as close as possible to equilateral. Known as the GradNormal algorithm, this method can produce a high-quality, smooth surface.

3. Methodology

3.1. Algorithm Pipeline

The algorithm pipeline is shown in Figure 1. For a dental scan as the input (a), our method starts with a preceding segmentation algorithm on the input model (b). Following this, a learning-based approach generates a point cloud to approximate the whole tooth (c). Then, an implicit surface reconstruction process (d) is conducted for subsequent steps. After this, the Restricted Voronoi Diagram (RVD) merges the generated dental root and the existing dental crown (e). Finally, the transition area is smoothed by solving a partial differential equation, resulting in a high-quality triangle surface (f).

3.2. Distinguishing Skirt of Crown

Common methods for obtaining oral models include intraoral scanning and oral impressions. However, due to limitations in device accuracy and imaging principles, capturing the gaps between teeth can be challenging. In such cases, tooth segmentation may result in a crown with a skirt, as shown in Figure 2. It is essential to identify the skirt portion from the oral scan, as this aids in the subsequent tooth completion and reconstruction process. More specifically, the task involves predicting the likelihood of a mesh vertex located in the skirt of a crown.

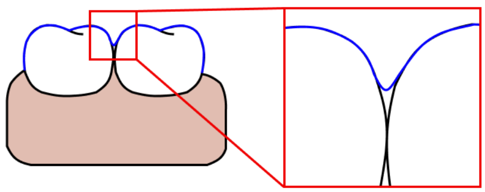

Figure 2. Illustration of the crown's skirt. The black lines represent the natural tooth shape, while the blue lines indicate the intraoral scan results. It is essential to predict the likelihood of a mesh vertex being located within the skirt of the crown.

Dataset. We collected 28 sets of crown models obtained through segmentation algorithms, along with their corresponding manually restored, morphologically complete tooth models. This dataset includes 200 sets of tooth data for both upper and lower jaws, with FDI labels ranging from 1 to 7, excluding data for wisdom teeth (FDI labeled 8). Since human teeth exhibit bilateral symmetry, we did not differentiate between corresponding teeth on the left and right sides in the training data. For each vertex on the crown, if there is a corresponding overlapping vertex in the restored model, it is labeled as a valid vertex with a confidence score of 1. Conversely, if there is no corresponding vertex, it is labeled as a skirt vertex with a confidence score of 0.

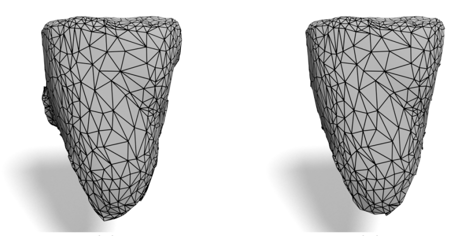

Figure 3. Effect of discard skirt vertices. (a) The original crown. (b) The crown mesh after skirt vertices being discard.

Classification. Based on the labeled data mentioned above, we use Diffusion Net [29] as the backbone network for training. Compared to the original diffusion net, we concatenate the hks features of the data with the xyz features for training, which achieved better results than using either hks features or xyz features alone. By applying the trained network onto the input dental crown mesh, we get the confidence of each vertex (or the probability of being a non-skirt vertex). Based on this, we can directly discard vertices with confidence below a given threshold (e.g., 0.5). Figure 3 shows a comparison between the original crown mesh and the crown mesh with the skirt vertices removed.

3.3. Tooth Point Cloud Completion

The shape completion task in this paper is to generate a complete tooth model that includes both the crown and the root. We accomplish this task at the point cloud level. Specifically, we first generate an augmented point cloud that potentially represents the completed tooth model.

Dataset To ensure data diversity, we collected 50 sets of complete tooth mesh models reconstructed based on the actual CBCT data. For each tooth set, the number of teeth ranges from 14 to 16, with 1 to 2 of them being wisdom teeth. We exclude wisdom teeth from our consideration. In the training phase, we first down-sample each tooth to 1024 points. For data augmentation, we introduce a factor α to specify the crown size. According to [26], The crown-to-root length ratio in adults varies slightly depending on the tooth type, but it is generally between 1:1 and 1:3. Considering factors such as crown wear and incomplete tooth eruption in practical situations, we have amplified this ratio to 1:7 during the data augmentation process. This means the crown can account for up to half of the total tooth length, and at least 1/8. If the crown length is further reduced, its eruption morphology becomes too small, resulting in incomplete morphological features that do not meet the requirements of the dataset. We restrict α in this range and randomly take six values. We can sort the sampled points along the dental growth axis so that part of the sampled points can be used to represent the dental crown according to the given α.

Training To this end, we obtained a tooth completion dataset containing 28 groups and $300 = 50 \times 6$ samples in each group. We leverage AdaPoinTr [40] as the backbone network to conduct the training process. Qualitative results are shown in Figure 8, and quantitative results are shown in Table 2. It can be observed that the network, being trained, can predict faithful complete teeth.

3.4. Implicit Reconstruction Based on Tetrahedral Tiling

Suppose we have a point cloud of a dental crown. Based on the discussion above, upon completion, we obtain a new point cloud P that encodes the entire tooth. The next step is to reconstruct the polygonal surface of the tooth. To our knowledge, Poisson reconstruction [16] is a competitive method among traditional reconstruction approaches, although the resulting mesh may suffer from poor triangulation quality. In contrast, GradNormal [14] has advantages in ensuring high triangulation quality. In this paper, we combine Poisson reconstruction and GradNormal to leverage the strengths of both methods.

Indicator function The essence of Poisson reconstruction [16] is to reconstruct the indicator function

$$\chi_M(p) = \begin{cases} 0, & p \notin M \\ 1, & p \in M \end{cases}$$

by solving Poisson's equation:

$$\Delta\chi = \nabla \cdot \vec{V},$$

where $\vec{V}$ is the vector field aligned with the normal vectors of the point cloud. To facilitate the Poisson reconstruction process, one must adapt the Octree to the sampling density.

The B-spline representation χ, coupled with the Octree, defines the finite element system used to approximate the indicator function. By default, the B-spline is of degree 3. Higher degrees allow for better approximation but may incur increased costs in space and time. It is important to note that the B-spline function can return an indicator value for any point (x, y, z). Instead of extracting the zero isosurface using Marching Cubes, we recommend employing a different isosurface extraction technique to achieve high-quality triangulations, where the iso-value is set to 0.5.

Establishing tetrahedral space We adopt the Goldberg tetrahedralization method for discreticizing the space [11]. As shown in Figure 4, we use a parameter e to control the tetrahedral meshing density. A smaller e results in denser space tiling and yields more accurate reconstruction results.

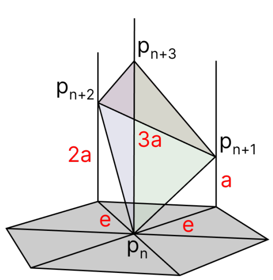

Figure 4. Goldberg tetrahedralization.

First, we partition the XOY plane using equilateral triangles with a side length of e. Then, we select one triangle and lift the three vertices by $a, 2a, 3a$, where $a = \sqrt{2}e/4$. After that, we tile the space using such a tetrahedral primitive.

Isosurface extraction Let T be one of the tetrahedral elements for tiling the whole space. T has six edges; for each edge, we deem the midpoint of this edge to be approximately lying on the underlying surface. In this way, one can construct a MidNormal mesh. After that, we can project each MidNormal mesh vertex to the closest point according to the implicit function χ. Finally, we remove all valence-four vertices by local edge flipping. The GradNormal algorithm generates a triangular mesh with angles between 35.2 and 101.5 degrees, thereby obtaining much higher triangle quality than Marching Cubes.

3.5. Crown-Root Integration

In the following, we will demonstrate how to retain the crown geometry and meshing topology by using the reconstructed outcome as the guiding surface.

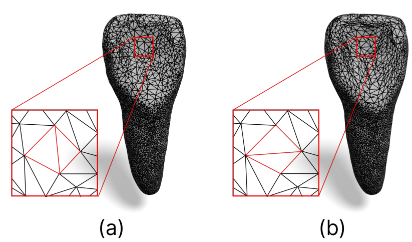

Figure 5. Generally speaking, by taking the original triangle mesh $M = (V, E, F)$ as the base surface, the restricted Voronoi diagram of V induces another triangle mesh M', where M is different from M'. (a) and (b) respectively show M and M'. If M' is identical to M, then M is strong-Delaunay.

Strong-Delaunay Generally speaking, by taking the original triangle mesh $M = (V, E, F)$ as the base surface, the restricted Voronoi diagram of V induces a different triangle mesh M'; See Figure 5. In the following, we first introduce a type of triangle mesh, referred to as a *strong-Delaunay* mesh in this paper.

Definition. Suppose we have a closed 2-manifold triangle mesh $M = (V, E, F)$. By taking the original triangle mesh as the base surface, the restricted Voronoi diagram of V induces another triangle mesh M'. We say that M is *strong-Delaunay* if M' is identical to M.

From the perspective of differential geometry, a sufficiently small local surface patch can be considered planar. In 2D Euclidean space, Delaunay triangulation precisely satisfies the property that the sum of a pair of edge-based opposite angles is equal to or less than π. Thus, Delaunay meshes [22] represent a special type of triangle mesh where the local Delaunay condition holds. However, for a curved shape in 3D, a Voronoi cell may intrude into the opposite side of a thin-plate structure, causing the input mesh surface M not to be strong-Delaunay. Therefore, it is evident that Delaunay meshes [22] is a necessary condition for being strong-Delaunay. Nonetheless, as long as the triangulation is sufficiently dense (by increasing the mesh resolution), Delaunay meshes will be strong-Delaunay.

In the subsequent mesh integration process, we combine the vertices of the crown mesh with those of the root mesh and perform an RVD partition on the guiding surface. Then, based on the dual relationship between RVD and Delaunay, we obtain the final integration result. Clearly, if the crown mesh M does not meet the Strong-Delaunay requirements, the topological relationship of the result cannot be guaranteed to be strictly consistent with the original crown mesh, and edge flips may occur, as shown in Figure 5.

Two conditions To determine whether a triangle mesh is strong-Delaunay, the above definition uses the original triangle mesh as the base surface. Introducing a sufficiently small perturbation to the base surface or using a slightly different one will allow a strong-Delaunay mesh to maintain its meshing topology even with the new base surface. Thus, it follows that the meshing topology of the crown part can be preserved as long as the following two conditions are satisfied:

1. The guiding surface is sufficiently close to the original crown.
2. The mesh surface of the original crown is strong-Delaunay.

Our algorithm is based precisely on these two conditions.

Algorithm for preserving crown Based on the above discussion, there are two key points for restoring the crown. Firstly, since the reconstructed outcome must differ from the original crown, we sample additional points from the original crown before running the Poisson reconstruction solver. Simultaneously, we need to increase the resolution of the tetrahedral tiling so that each tetrahedral element is sufficiently small. Secondly, we add edge-based Steiner points to the original crown model to ensure it becomes a Delaunay mesh, which can be achieved by utilizing Liu et al.'s algorithm [22].

Recall that we have a complete point cloud (including the crown part V_1 and the root part V_2), as well as a reconstructed surface M. Details on separating the crown from the root part will be elaborated on later. We combine the points in V_2 with the vertices of the original crown to yield a vertex set V. We then compute the restricted Voronoi decomposition of M, with V serving as the point set. The dual of the resulting RVD produces a triangle mesh that preserves the vertices and connections of the original crown. Figure 6 illustrates the original crown and the resulting completed mesh, demonstrating that our approach effectively retains the crown geometry and meshing topology.

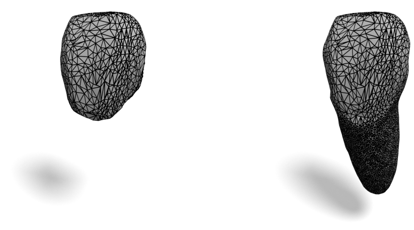

Figure 6. Our completion algorithm can retain the geometry and meshing topology of the original crown model. (a) The original crown. (b) The resulting completed mesh.

3.6. More Implementation Details

Tetrahedral tiling resolution As mentioned above, the guiding surface must adequately fit the original crown model. Therefore, we need to adjust the tetrahedral tiling resolution by controlling the value of e. Below are the distances between the original mesh vertices and the reconstructed surface for different values of e. From the data in Table 1, it is clear that as e decreases, the distance from the vertices on the original crown mesh to the reconstructed mesh also decreases, indicating improved adherence of the reconstructed mesh to the original crown. In our implementation, we set e to 0.5 to achieve a desirable fit.

e	1.0	0.75	0.5	0.25
$d_{\mathbf{avg}}$	$3.17e^{-2}$	$2.29e^{-2}$	$1.41e^{-2}$	$7.10e^{-3}$
$d_{\mathbf{max}}$	0.29	0.26	0.16	0.12

Table 1. For various values of e, we record the distances between the crown and the reconstructed outcome.

Separation between the crown and the root Let M be the reconstructed complete tooth shape while M_{crown} be the original crown. Let l be the dental growth axis. For a vertex $v \in M$, if v satisfies

$$\|v - v'\| > \epsilon$$

or

$$\|v - v'\| \leq \epsilon \quad \text{and} \quad (v' - v) \cdot l > 0,$$

for every vertex v' in the crown M_{crown}, then we label $v \in M$ with 'Root_Vert'. Otherwise, we label v with 'Crown_Vert'. The vertices in M are thus classified into two groups.

Delaunay mesh We use $l_{\min}$ to denote the length of the shortest edge in the mesh M, and $\theta_{\min}$ to represent the smallest interior angle of the mesh. By adding Steiner points onto edges, we can obtain a Delaunay mesh. The key points for adding auxiliary points include:

1. For the edge $e = (v_1, v_2) \in M$, the two closest auxiliary points s_1 and s_2 to the endpoints of the edge are at a distance of ρ_v:

$$\rho_v = \min \left\{ \frac{l_{\min} \sin \theta_{\min}}{0.5 + \sin \theta_{\min}}, \frac{l_{\min}}{2} \right\}.$$

2. For any two adjacent auxiliary points s_i and s_j on the edge e, the minimum gap ρ_e between s_i and s_j satisfies

$$\rho_e \leq 2\rho_v \sin \theta_{\min}.$$

Transition optimization Recall that we have a step to restore the crown from the guiding surface. This process may lead to a non-smooth transition between the crown and the root. Additionally, since the crown typically has skirts, this further intensifies the non-smooth effects. We employ the commonly used biharmonic smoothing technique to achieve a natural transition. After identifying the transition area, we optimize the vertex locations by solving the equation

$$L^2 \boldsymbol{x} = \boldsymbol{0},$$

where L is the Laplacian operator. Figure 7 illustrates the smoothing effect.

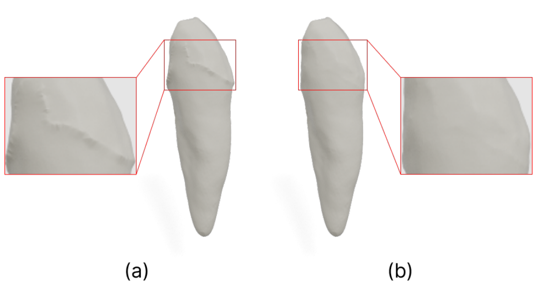

Figure 7. Smoothing effect. We retain the crown and root parts, while applying biharmonic smoothing to the transition area between them.

4. Experiments

4.1. Experimental Setting

Training setting Our training environment utilized the PyTorch framework with an NVIDIA GTX 3090 Ti GPU. The training was conducted for 100 epochs, using all other default settings from the AdaPoinTr [40] configurations on the PCN dataset [41]. The dataset was split into a training set and a test set with a 4:1 ratio. After training, we conducted tests on dental scan data without ground truth.

Evaluation metric We follow existing approaches [41, 33] and use the mean Chamfer Distance as the evaluation metric, which measures the distance between the predicted point cloud and the ground truth at the set level. For each prediction, the Chamfer Distance between the predicted point set P and the ground truth point set G is calculated as follows:

$$\begin{aligned} \text{Chamfer}\,(P, G) = & \frac{1}{2|P|} \sum_{p \in P} \min_{g \in G} ||p - g|| \\ & + \frac{1}{2|G|} \sum_{g \in G} \min_{p \in P} ||p - g||. \end{aligned}$$

More specifically, we follow previous methods to use the L2 norm to calculate the distance between two points and then compute the Chamfer Distance. Additionally, following [32], we employ the F-Score as another evaluation metric. Both metrics assess the adherence between the completion results and the ground truth.

Evaluation data The number of vertices and triangles in the intraoral scan data used in this experiment ranged from 100K to 150K, all acquired from commonly available intraoral scanners on the market.

4.2. Tooth Point Cloud Completion

We report the quantitative results of the tooth point cloud completion test in Table 2, using the F-Score and CD_{l2} (multiplied by 1000). Additionally, the qualitative results are presented in Figure 8.

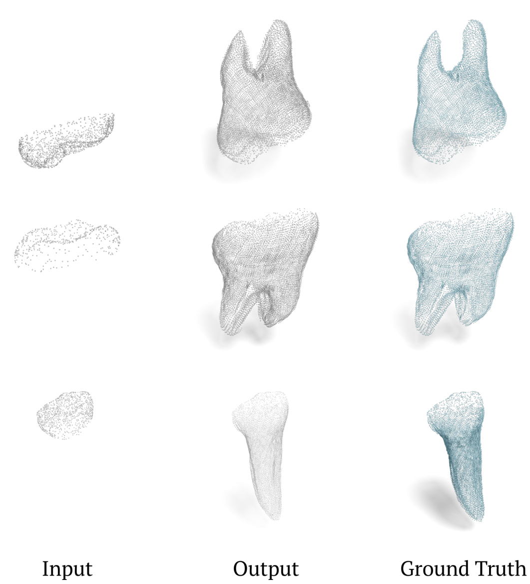

Figure 8. Qualitative results on our dataset.

	F-Score ↑	**CD** l_2 ↓
Avg	0.58	0.37

Table 2. Quantitative results on our dataset.

As demonstrated by the data in the images and tables above, our point cloud completion algorithm can generate point cloud data with realistic shapes for various types of teeth, showing high similarity to the ground truth. Subsequent experiments further validate the effectiveness of the algorithm.

4.3. Mesh Reconstruction Quality

In this paper, we evaluate the quality of grid triangulation using five metrics: the average quality of triangles Q_{avg}, the minimum quality of triangles $Q_{\min}$, the average value of the minimum angles of triangles θ_{avg}, the minimum value of angles $\theta_{\min}$, and the percentage of angles less than 30° among all triangle angles, denoted as $\%_{30^\circ}$. The quality of a triangle is calculated using the following formula:

$$Q_t = \frac{6S_t}{\sqrt{3}p_t h_t},$$

where S_t represents the area of the triangle, p_t represents the semi-perimeter, and h_t represents the length of the longest side. For equilateral triangles, the quality Q_t equals 1, and as the triangle becomes more elongated, the value of Q_t decreases.

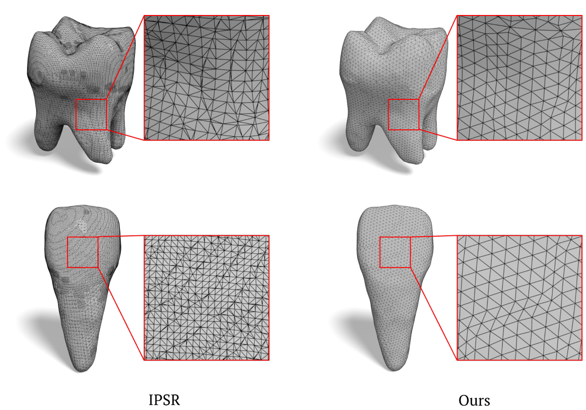

Figure 9. Facet details of reconstructed models.

We compare the proposed reconstruction method in this paper with the Iterative Poisson Surface Reconstruction algorithm (IPSR) [15]. Visualization of the quality results and statistical data is provided in Figure 9, Figure 13 and Table 5, respectively.

The data above demonstrate that the method proposed in this paper produces a more uniformly triangulated mesh, with shapes that are closer to equilateral triangles. This results in higher quality in mesh reconstruction, contributing to improved geometric fidelity and overall performance in applications requiring precise modeling.

4.4. Mesh Integration

The objective of the method proposed in this paper is to preserve the morphology of the original tooth crown mesh as much as possible while removing unreasonable overhanging edges during the integration process. In this experiment, we performed vertex sampling on the original tooth crown model M_c, selecting $p_i \in M_c$, and calculated the Euclidean distance d_i from each sampled vertex to the fused result surface M. The number of vertices in different distance intervals is shown in Table 3.

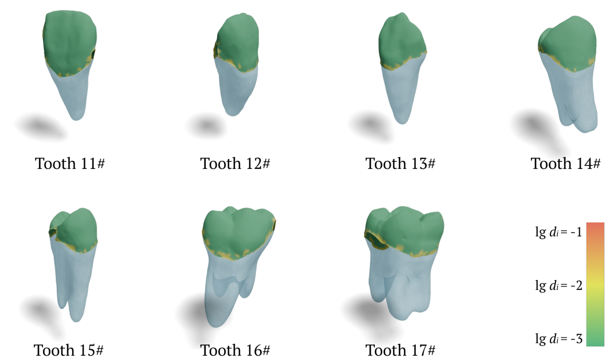

Figure 10. Our complete outcomes, where the difference (of the crown part) due to the completion operation is visualized in a color-coded style.

	Total	$[0, 1e^{-3}]$	$(1e^{-3}, 1e^{-2}]$	$(1e^{-2}, 1e^{-1}]$
11#	1828	1435	393	0
12#	1455	1116	328	11
13#	1522	1235	287	0
14#	1907	1598	309	0
15#	2116	1759	354	3
16#	2091	1693	392	6
17#	2080	1763	315	2

Table 3. Statistics for comparing the original crown and the integration outcome, using the models shown in Figure 10 for testing. The numbers in the table represent the quantity of vertices p_i in different distance intervals, where $p_i \in M_c$.

In the experimental results mentioned above, it can be observed that our algorithm effectively preserves the vertex positions and topological connections of the original dental crown mesh in the occlusal, labial, and lingual areas, with only minor errors likely due to floating-point precision. Recall that we initially discard vertices that are obviously located in the skirt area, which helps generate more accurate shape completion results.

Additionally, even if these skirt vertices were not completely eliminated during the initial mesh processing, their adverse influence on shape integration will be addressed in the subsequent optimization process. In the step of computing RVDs, vertices far from the guiding surfaces do not contribute to the surface dominance and are thus naturally eliminated.

4.5. Robust and Efficiency

Extensive tests with diverse data from individuals of different ages and sexes validate the robustness of our proposed algorithm. Additionally, it is capable of processing uncommon tooth shapes, such as decayed, worn, and attached teeth, as well as deciduous teeth, overly small teeth, and other special cases.

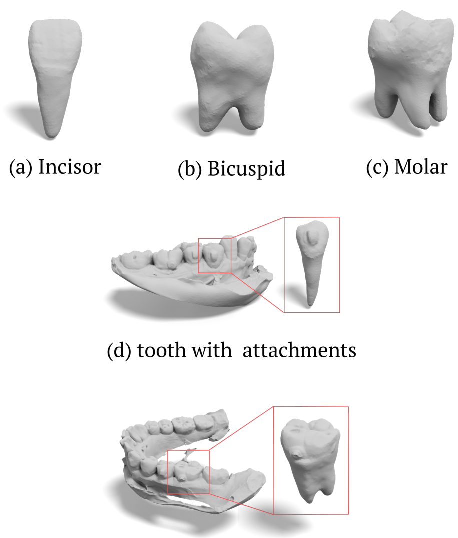

(a) Incisor (b) Bicuspid (c) Molar

(d) tooth with attachments

(e) Worn tooth with bracket

Figure 11. Diverse tooth completion cases.

	$e = 1.0$	$e = 0.75$	$e = 0.5$
Teeth Set 1#	8.73s	11.57s	14.37s
Teeth Set 2#	8.53s	11.17s	13.87s
Teeth Set 3#	8.82s	12.22s	15.13s
Teeth Set 4#	8.26s	11.12s	14.07s

Table 4. Runtime efficiency

We adjusted the tetrahedral tiling resolutions to different levels, with the average processing time for a single tooth shown in Table 4. It is evident that as the resolution increases, our algorithm achieves higher reconstruction accuracy but requires more time. Although reducing the resolution (which means a higher e value) can improve the efficiency of our algorithm, a resolution that is too low may cause a significant difference between the guiding surface and the original crown mesh, leading to vertex loss on the crown during the mesh merging process. Therefore, we need to strike a balance between performance and accuracy. In our implementation, we choose $e = 0.5$ as the commonly used resolution.

Additionally, parallel computation techniques can be employed for further optimization, enhancing performance in practical applications. More experimental results are presented in Figure 14.

4.6. User Feedback

Given the specific context of dental modeling, evaluating its performance necessitates participants with a background in dental medicine. In this user study, we invited several experienced dental technicians, each with years of professional experience, to score the generation and integration outcomes for over 50 sets of data, comprising approximately 1,300 teeth.

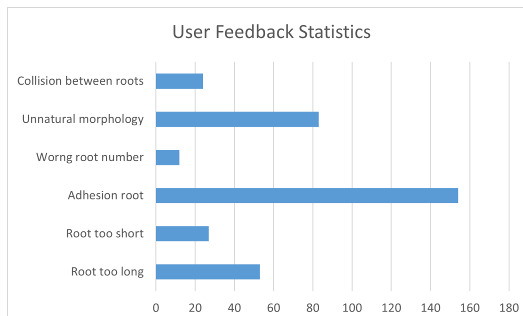

Figure 12. User feedback statistics, the statistics in the table represent the frequency of user-reported instances for each issue.

From Figure 12, it is evident that the participants are satisfied with our completed outcomes, particularly noting that our algorithm can preserve the crown, unlike existing algorithms. However, they believe there is still room for improvement, specifically at the base of multi-rooted teeth. In the future, we will collect more data and focus on the generation of multi-rooted teeth.

5. Conclusion

In this paper, we introduce an algorithmic framework for completing a tooth model from a dental crown. The main advantage of our algorithm is its ability to preserve not only the geometry and mesh topology of the original dental crown but also the overall triangulation quality and natural shape. Specifically, we present several contributions: First, we combine Poisson reconstruction with GradNormal to leverage the strengths of both methods. Second, we discuss a type of strong-Delaunay mesh and provide an algorithm that preserves the geometry and mesh topology of the given part while addressing the shape completion problem. Last but not least, we utilize biharmonic smoothing to achieve a natural transition between the crown and root, enhancing the shape appearance of the completed teeth. Extensive experiments validate the effectiveness of the proposed algorithm.

Acknowledgement

The authors would like to thank the anonymous reviewers for their valuable comments and suggestions. This work is supported by National Natural Science Foundation of China (62272277, U23A20312).

References

[1] F. Bernardini, J. Mittleman, H. Rushmeier, C. Silva, and G. Taubin. The ball-pivoting algorithm for surface reconstruction. *IEEE transactions on visualization and computer graphics*, 5(4):349–359, 1999. 3

[2] S. Bischoff, D. Pavic, and L. Kobbelt. Automatic restoration of polygon models. *ACM Transactions on Graphics (TOG)*, 24(4):1332–1352, 2005. 2

[3] M. Centin, N. Pezzotti, and A. Signoroni. Poisson-driven seamless completion of triangular meshes. *Computer Aided Geometric Design*, 35:42–55, 2015. 2

[4] L. Chen and M. Holst. Efficient mesh optimization schemes based on optimal delaunay triangulations. *Computer Methods in Applied Mechanics and Engineering*, 200(9-12):967–984, 2011. 3

[5] Z. Chen, J. Cao, and W. Wang. Isotropic surface remeshing using constrained centroidal delaunay mesh. In *Computer Graphics Forum*, volume 31, pages 2077–2085. Wiley Online Library, 2012. 3

[6] X.-X. Cheng, X.-M. Fu, C. Zhang, and S. Chai. Practical error-bounded remeshing by adaptive refinement. *Computers & Graphics*, 82:163–173, 2019. 3

[7] Z. Cui, C. Li, N. Chen, G. Wei, R. Chen, Y. Zhou, D. Shen, and W. Wang. Tsegnet: An efficient and accurate tooth segmentation network on 3d dental model. *Medical Image Analysis*, 69:101949, 2021. 2

[8] F. Dassi, A. Mola, and H. Si. Curvature-adapted remeshing of cad surfaces. *Procedia Engineering*, 82:253–265, 2014. 3

[9] Q. Du, V. Faber, and M. Gunzburger. Centroidal voronoi tessellations: Applications and algorithms. *SIAM review*, 41(4):637–676, 1999. 3

[10] M. Dunyach, D. Vanderhaeghe, L. Barthe, and M. Botsch. Adaptive remeshing for real-time mesh deformation. In *Eurographics 2013*. The Eurographics Association, 2013. 3

[11] D. Eppstein, J. M. Sullivan, and A. Üngör. Tiling space and slabs with acute tetrahedra. *Computational Geometry*, 27(3):237–255, 2004. 5

[12] J. Guo, D.-M. Yan, X. Jia, and X. Zhang. Efficient maximal poisson-disk sampling and remeshing on surfaces. *Computers & Graphics*, 46:72–79, 2015. 3

[13] G. Harary, A. Tal, and E. Grinspun. Context-based coherent surface completion. *ACM Transactions on Graphics (TOG)*, 33(1):1–12, 2014. 2

[14] J. Hass and M. Trnkova. Approximating isosurfaces by guaranteed-quality triangular meshes. In *Computer Graphics Forum*, volume 39, pages 29–40. Wiley Online Library, 2020. 3, 5

[15] F. Hou, C. Wang, W. Wang, H. Qin, C. Qian, and Y. He. Iterative poisson surface reconstruction (ipsr) for unoriented points. *arXiv preprint arXiv:2209.09510*, 2022. 3, 8

[16] M. Kazhdan, M. Bolitho, and H. Hoppe. Poisson surface reconstruction. In *Proceedings of the fourth Eurographics symposium on Geometry processing*, volume 7, 2006. 3, 4, 5

[17] M. Kazhdan and H. Hoppe. Screened poisson surface reconstruction. *ACM Transactions on Graphics (ToG)*, 32(3):1–13, 2013. 3

[18] D. Khan, D.-M. Yan, S. Gui, B. Lu, and X. Zhang. Molecular surface remeshing with local region refinement. *International journal of molecular sciences*, 19(5):1383, 2018. 3

[19] P. Lancaster and K. Salkauskas. Surfaces generated by moving least squares methods. *Mathematics of computation*, 37(155):141–158, 1981. 3

[20] J. Lin, X. Jin, C. Wang, and K.-C. Hui. Mesh composition on models with arbitrary boundary topology. *IEEE transactions on visualization and computer graphics*, 14(3):653–665, 2008. 2

[21] M. Liu, X. Li, J. Liu, W. Liu, and Z. Yu. Tucnet: A channel and spatial attention-based graph convolutional network for teeth upsampling and completion. *Computers in Biology and Medicine*, 166:107519, 2023. 2, 3

[22] Y.-J. Liu, C.-X. Xu, D. Fan, and Y. He. Efficient construction and simplification of delaunay meshes. *ACM Transactions on Graphics (TOG)*, 34(6):1–13, 2015. 5, 6

[23] M. Ma, X. Yu, N. Lei, H. Si, and X. Gu. Guaranteed quality isotropic surface remeshing based on uniformization. *Procedia engineering*, 203:297–309, 2017. 3

[24] M. Martorelli and P. Ausiello. A novel approach for a complete 3d tooth reconstruction using only 3d crown data. *International Journal on Interactive Design and Manufacturing (IJIDeM)*, 7:125–133, 2013. 2

[25] H. Nguyen, J. Burkardt, M. Gunzburger, L. Ju, and Y. Saka. Constrained cvt meshes and a comparison of triangular mesh generators. *Computational geometry*, 42(1):1–19, 2009. 3

[26] R. G. Phulari. *Textbook of dental anatomy, physiology and occlusion*. JP Medical Ltd, 2013. 4

[27] J. Qian, Y. Gao, Y. Tang, Y. Tao, J. Lin, and H. Lin. An automatic algorithm for repairing dental models based on contours. In *Tenth international conference on graphics and image processing (ICGIP 2018)*, volume 11069, pages 299–307. SPIE, 2019. 3

[28] E. Ruiz-Gironés, J. Sarrate, and X. Roca. Generation of curved high-order meshes with optimal quality and geometric accuracy. *Procedia engineering*, 163:315–327, 2016. 3

[29] N. Sharp, S. Attaiki, K. Crane, and M. Ovsjanikov. Diffusionnet: Discretization agnostic learning on surfaces. *ACM Transactions on Graphics (TOG)*, 41(3):1–16, 2022. 4

[30] E. Taneva, B. Kusnoto, and C. A. Evans. 3d scanning, imaging, and printing in orthodontics. *Issues in contemporary orthodontics*, 148(5):862–7, 2015. 1

[31] N. E. Tarraf and D. M. Ali. Present and the future of digital orthodontics. In *Seminars in Orthodontics*, volume 24, pages 376–385. Elsevier, 2018. 1

[32] M. Tatarchenko, S. R. Richter, R. Ranftl, Z. Li, V. Koltun, and T. Brox. What do single-view 3d reconstruction networks learn? In *Proceedings of the IEEE/CVF conference on computer vision and pattern recognition*, pages 3405–3414, 2019. 7

[33] L. P. Tchapmi, V. Kosaraju, H. Rezatofighi, I. Reid, and S. Savarese. Topnet: Structural point cloud decoder. In *Proceedings of the IEEE/CVF conference on computer vision and pattern recognition*, pages 383–392, 2019. 7

[34] X. Wang, X. Liu, L. Lu, B. Li, J. Cao, B. Yin, and X. Shi. Automatic hole-filling of cad models with feature-preserving. *Computers & Graphics*, 36(2):101–110, 2012. 2

[35] W.-C. Xie and X.-F. Zou. A triangulation-based hole patching method using differential evolution. *Computer-Aided Design*, 45(12):1651–1664, 2013. 2

[36] L. Xing, X. Zhang, C. C. Wang, and K.-C. Hui. Highly parallel algorithms for visual-perception-guided surface remeshing. *IEEE computer graphics and applications*, 34(1):52–64, 2013. 3

[37] X. Xu, C. Liu, and Y. Zheng. 3d tooth segmentation and labeling using deep convolutional neural networks. *IEEE transactions on visualization and computer graphics*, 25(7):2336–2348, 2018. 2

[38] D.-M. Yan, B. Lévy, Y. Liu, F. Sun, and W. Wang. Isotropic remeshing with fast and exact computation of restricted voronoi diagram. In *Computer graphics forum*, volume 28, pages 1445–1454. Wiley Online Library, 2009. 3

[39] D.-M. Yan and P. Wonka. Non-obtuse remeshing with centroidal voronoi tessellation. *IEEE Transactions on Visualization and Computer Graphics*, 22(9):2136–2144, 2015. 3

[40] X. Yu, Y. Rao, Z. Wang, J. Lu, and J. Zhou. Adapointr: Diverse point cloud completion with adaptive geometry-aware transformers. *IEEE Transactions on Pattern Analysis and Machine Intelligence*, 2023. 3, 4, 7

[41] W. Yuan, T. Khot, D. Held, C. Mertz, and M. Hebert. Pcn: Point completion network. In *2018 international conference on 3D vision (3DV)*, pages 728–737. IEEE, 2018. 7

[42] S. Zhang, W. Wu, W. Wei, et al. An intelligent identification and repair method for annular holes in 3d printing. *Computational Intelligence and Neuroscience*, 2022, 2022. 2

[43] M. Zhao, L. Ma, W. Tan, and D. Nie. Interactive tooth segmentation of dental models. In *2005 IEEE Engineering in Medicine and Biology 27th Annual Conference*, pages 654–657. IEEE, 2006. 1

[44] K. Zhou, M. Gong, X. Huang, and B. Guo. Data-parallel octrees for surface reconstruction. *IEEE transactions on visualization and computer graphics*, 17(5):669–681, 2010. 3

[45] H. Zhu, X. Jia, C. Zhang, and T. Liu. Toothcr: a two-stage completion and reconstruction approach on 3d dental model. In *Pacific-Asia Conference on Knowledge Discovery and Data Mining*, pages 161–172. Springer, 2022. 2, 3

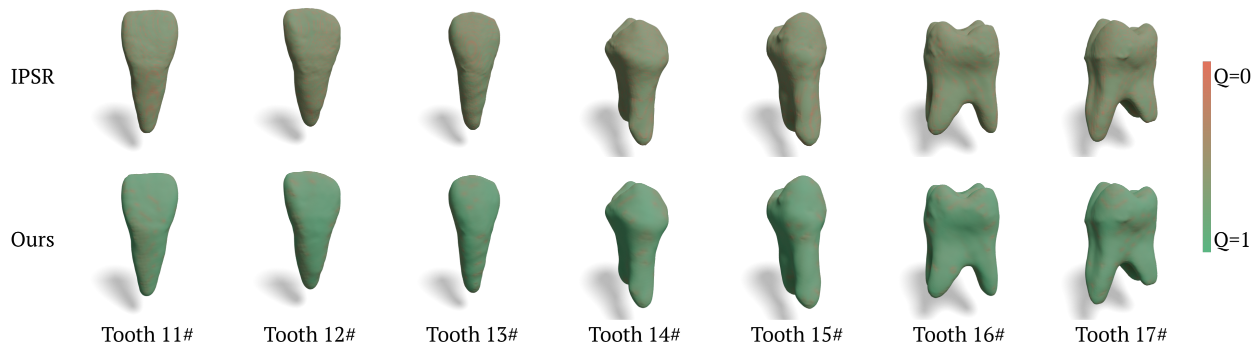

Figure 13. Qualitative results on triangulation quality. The greener areas indicate higher triangulation quality, while the redder areas indicate lower quality.

	Tooth	$Q_{\textbf{avg}}$	$Q_{\min}$	$\theta_{\textbf{avg}}$	$\theta_{\min}$	$\%_{<30^\circ}$
IPSR	11	0.60	$1.60e^{-4}$	32.23	$5.37e^{-3}$	39.62%
Ours	11	0.84	$8.75e^{-2}$	48.67	4.47	2.82%
IPSR	12	0.61	$7.25e^{-5}$	32.07	$5.06e^{-3}$	40.01%
Ours	12	0.85	$1.02e^{-2}$	48.83	0.58	2.82%
IPSR	13	0.61	$6.42e^{-4}$	32.43	$1.61e^{-2}$	38.70%
Ours	13	0.84	$6.27e^{-2}$	48.37	3.75	3.10%
IPSR	14	0.60	$1.53e^{-4}$	31.98	$1.66e^{-2}$	40.27%
Ours	14	0.85	$3.43e^{-2}$	49.04	1.94	2.60%
IPSR	15	0.60	$2.32e^{-4}$	32.12	$1.34e^{-2}$	39.49%
Ours	15	0.85	$4.66e^{-2}$	48.82	2.61	2.87%
IPSR	16	0.61	$2.57e^{-5}$	32.58	$1.04e^{-2}$	38.26%
Ours	16	0.85	$1.67e^{-2}$	48.90	1.04	2.80%
IPSR	17	0.61	$7.25e^{-6}$	32.38	$6.01e^{-3}$	38.77%
Ours	17	0.85	$1.83e^{-3}$	48.97	1.12	3.09%

Table 5. Quantitative results on triangulation quality.

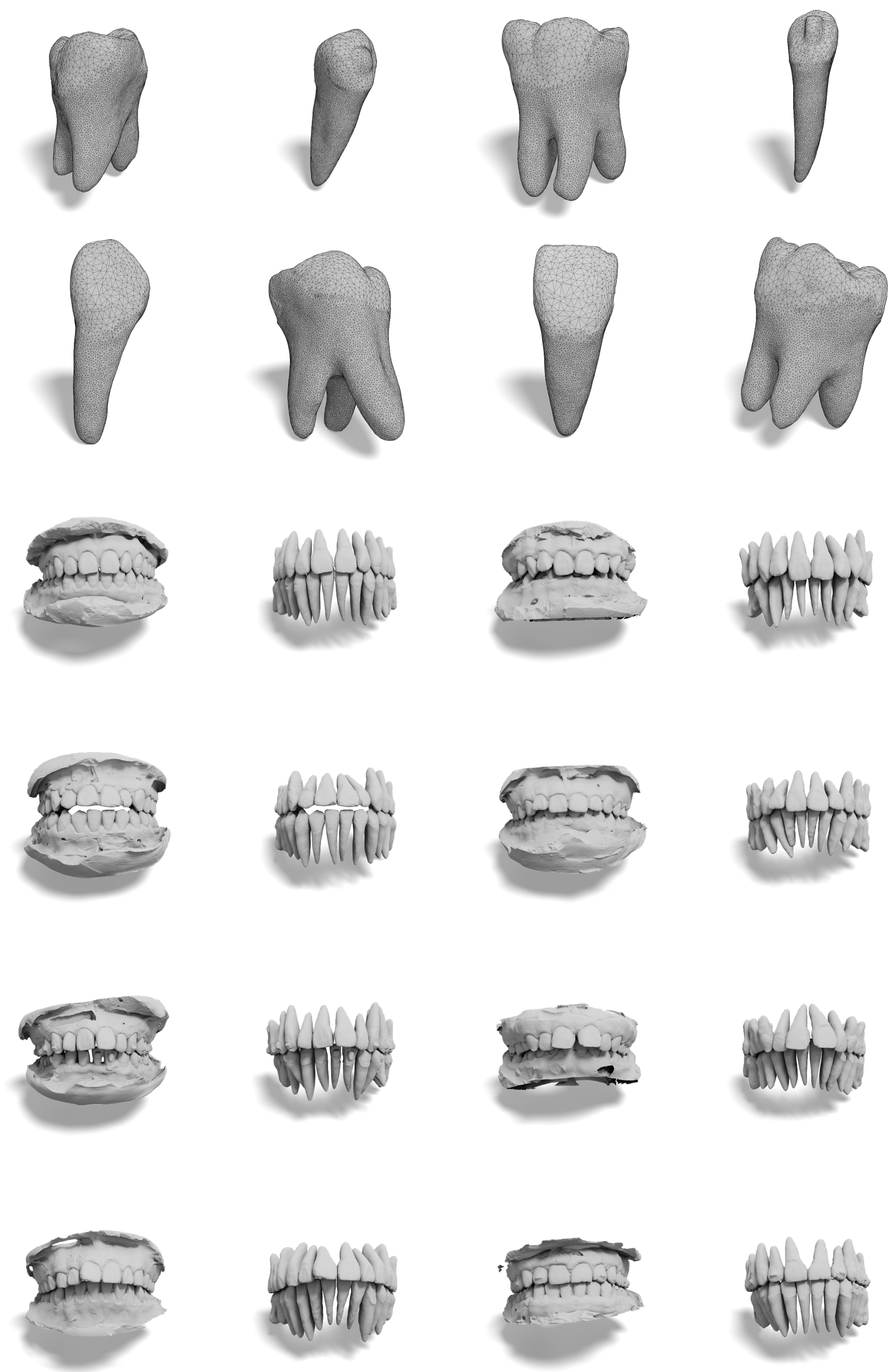

Figure 14. More experimental results.